Nano-Micro Letters

e-ISSN 2150-5551
CN 31-2103/TB

ARTICLE

https://doi.org/10.1007/s40820-022-00891-9

Cite as
Nano-Micro Lett.
(2022) 14:144

Received: 28 May 2022
Accepted: 17 June 2022
Published online: 15 July 2022

Oxygen Vacancy-Rich 2D TiO_2 Nanosheets: A Bridge Toward High Stability and Rapid Hydrogen Storage Kinetics of Nano-Confined MgH_2

Li Ren[1,2,3], Wen Zhu[1], Yinghui Li[1], Xi Lin[1], Hao Xu[1], Fengzhan Sun[1], Chong Lu[4], Jianxin Zou[1,2,3] ✉

HIGHLIGHTS

- A MgH_2/TiO_2 heterostructure with nano MgH_2 assembled on oxygen vacancy-rich 2D TiO_2 nanosheets was successfully fabricated via a simple solvothermal strategy.
- The MgH_2/TiO_2 heterostructure shows rapid desorption kinetics, low dehydrogenation temperature, and excellent cycling stability.
- In situ HRTEM observations and ex situ XPS analyses reveal that multi-valance of Ti species, presence of abundant oxygen vacancies, formation of catalytic Mg-Ti oxides, and confinement of TiO_2 nanosheets, contribute to the high stability and kinetically accelerated hydrogen sorption performances of Mg.

ABSTRACT MgH_2 has attracted intensive interests as one of the most promising hydrogen storage materials. Nevertheless, the high desorption temperature, sluggish kinetics, and rapid capacity decay hamper its commercial application. Herein, 2D TiO_2 nanosheets with abundant oxygen vacancies are used to fabricate a flower-like MgH_2/TiO_2 heterostructure with enhanced hydrogen storage performances. Particularly, the onset hydrogen desorption temperature of the MgH_2/TiO_2 heterostructure is lowered down to 180 °C (295 °C for blank MgH_2). The initial desorption rate of MgH_2/TiO_2 reaches 2.116 wt% min^{-1} at 300 °C, 35 times of the blank MgH_2 under the same conditions. Moreover, the capacity retention is as high as 98.5% after 100 cycles at 300 °C, remarkably higher than those of the previously reported MgH_2-TiO_2 composites. Both in situ HRTEM observations and ex situ XPS analyses confirm that the synergistic effects from multi-valance of Ti species, accelerated electron transportation caused by oxygen vacancies, formation of catalytic Mg-Ti oxides, and stabilized MgH_2 NPs confined by TiO_2 nanosheets contribute to the high stability and kinetically accelerated

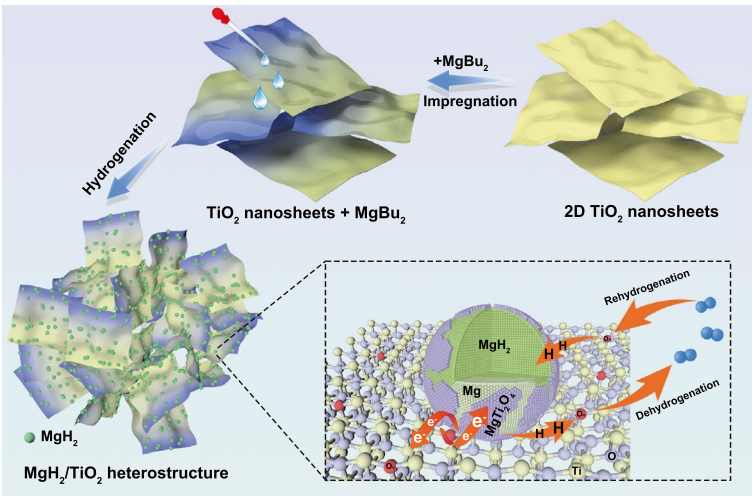

✉ Jianxin Zou, zoujx@sjtu.edu.cn
[1] National Engineering Research Center of Light Alloys Net Forming & State Key Laboratory of Metal Matrix Composites, Shanghai Jiao Tong University, Shanghai 200240, People's Republic of China
[2] Shanghai Engineering Research Center of Mg Materials and Applications & School of Materials Science and Engineering, Shanghai Jiao Tong University, Shanghai 200240, People's Republic of China
[3] Center of Hydrogen Science, Shanghai Jiao Tong University, Shanghai 200240, People's Republic of China
[4] Instrumental Analysis Center of SJTU, Shanghai Jiao Tong University, Shanghai 200240, People's Republic of China

hydrogen storage performances of the composite. The strategy of using 2D substrates with abundant defects to support nano-sized energy storage materials to build heterostructure is therefore promising for the design of high-performance energy materials.

KEYWORDS Hydrogen storage; MgH_2; TiO_2 nanosheets; Oxygen vacancies; Nanoconfinement

1 Introduction

With the ever-increasing global energy demands and environmental concerns, clean and renewable energy is urgently demanded worldwide. Hydrogen has been considered as one of the most promising candidates to alternate fossil fuels, due to its intrinsic clean nature, environmental-friendliness, and high gravimetric energy density (142 MJ kg^{-1}) [1–4]. However, an effective strategy to store hydrogen is essential to realizing the "hydrogen economy" [5, 6]. Compared with hydrogen storage in pressurized tanks or cryogenic containers, solid-state hydrogen storage methods potentially have the advantages of high safety, low cost, and exceptional hydrogen storage capacity [7]. Among various solid-state hydrogen storage materials, magnesium hydride (MgH_2) has attracted tremendous attention, due to its high gravimetric (~ 7.6 wt% H_2) and volumetric (~ 110 kg m^{-3} H_2) hydrogen storage density, excellent reversibility, low cost, and nontoxicity [8, 9]. Unfortunately, the industrial application of MgH_2 has been seriously hampered by its high operating temperature and slow de/re-hydrogenation kinetics. Particularly, a high temperature of at least 280 °C is required at 1 bar for desorption of coarse-grained MgH_2, which far exceeds the working temperature of the proton exchange membrane fuel cell (PEMFC). Consequently, it is essential to improve the hydrogen storage performances of MgH_2 for possible applications in the hydrogen energy field.

In the last few decades, extensive researches have been executed toward fabricating novel Mg-based hydrogen storage materials with enhanced performances, such as adding catalysts [10–13], alloying [14–16], and reducing the particle size of MgH_2 [17–19]. From the extrinsic perspective, the use of additives to weaken the Mg-H bonding and promote the diffusion rate of hydrogen atoms, thus reducing the dehydrogenation temperature and accelerating the desorption rates, is regarded as an efficient strategy for enhancing the hydrogen desorption properties of MgH_2. These additives include transition metals (TM) [20, 21], transition metal oxides [22, 23], nitrides [24, 25], halides [26, 27], and hydrides [28, 29]. Among them, transition metals (Ti, V, Nb, Ni, Co) and their compounds (TiO_2, Nb_2O_5, V_2O_3) strike more attentions and have been proven to be the most effective additives to ameliorate the hydrogen sorption performances of MgH_2, since transition metals with multiple valences favor the electron transfer during the de/re-hydrogenation processes [26]. The Fermi level of transition metals is located around s-type orbitals, which is a necessary condition to promote hydrogen dissociation and recombination [30]. Cui et al. [21] systematically investigated the catalytic mechanism of TM on the MgH_2 by the synthesis of core (Mg)-shell (TM) structure. The results show that Mg-Ti composites, which can release hydrogen even under 200 °C, exhibit optimal desorption performances, owing to the lower electronegativity of Ti. Notably, it has been proved that TiO_2 possesses a superior catalytic effect than metallic Ti [31]. Furthermore, TiO_2 has many advantages, such as high natural abundance, low cost, and nontoxicity. Though the addition of catalysts through simple ball milling method can indeed ameliorate the kinetics of MgH_2 to some extent, the improvement is restricted by the inevitable self-aggregation and growth of the additives during cycling, as well as the low density of exposed active sites.

On the other hand, from an intrinsic point of view, nano-sized MgH_2, which owes the shortened diffusion path for hydrogen atoms and increased active sites for re/de-hydrogenation, has been successfully synthesized through various nanotechnologies, giving rise to improved hydrogen storage performances. For instance, the nano-confinement method has been proved to be a facile strategy to simultaneously improve the thermodynamics and kinetics of MgH_2 while reducing the capacity loss as little as possible. Nano-sized MgH_2 confined into porous carbon has demonstrated a noticeable decrease in its initial desorption temperature (~ 90 °C) compared with its bulk counterpart [32]. Yu et al. [33] synthesized Ni nanocrystal-decorated MgH_2 nanoparticles anchored on graphene sheets that exhibit excellent hydrogen sorption properties. The composites absorb 5.4 wt% H_2 within 10 min at 200 °C, and identical capacity can be released at the same temperature within 150 min. It is noted, however, that neither graphene nor porous carbon possesses good catalytic activities, and additional catalysts are needed to further improve hydrogen storage performances

 https://doi.org/10.1007/s40820-022-00891-9

of MgH_2. Although huge achievements have been achieved, it is still far from enough to enhance the hydrogen storage performances of MgH_2 by solely depending on any methods mentioned above. In this respect, it is essential to fabricate MgH_2 with extraordinary hydrogen storage performances by taking full advantage of both the intrinsic (nano-size) and the extrinsic (catalyst addition) strategy.

Recently, graphene-like two-dimensional (2D) transition metal oxides have been extensively studied due to their potential in energy-related applications with high surface area and unique electronic/thermal properties [34–37]. However, preparing hydrogen storage composites composed of graphene-like 2D TiO_2 nanosheets (TiO_2 NS) and MgH_2 by a simple ball milling method would cause irreversible agglomeration of TiO_2 NS, leading to seriously reduced catalytic active sites and deterioration of various spectacular intrinsic properties of 2D materials [38]. Thus, the idea of fabricating MgH_2 (0D)/TiO_2 (2D) heterostructure using graphene-like 2D TiO_2 NS is triggered as it can not only facilitate the formation of nano-sized MgH_2 through the confinement effect of TiO_2 NS but also possess catalytic effect for MgH_2. More importantly, the construction of MgH_2/TiO_2 heterostructure can effectively inhibit the self-stacking of TiO_2 layers, leading to increased surface catalytic sites for MgH_2. Additionally, defect engineering has also aroused more attention to adjusting the band structure and providing more catalytic active sites [39]. Among them, oxygen vacancy-rich TiO_2 has been proved to remarkably promote electron transportation, enhance electrical conductivity, and provide more active sites for the capture and diffusion of hydrogen [40, 41].

In light of the above consideration, herein, taking full advantage of the intrinsic (nano-size) and extrinsic (catalyst addition) effects, we report a first attempt to design a novel self-assembled MgH_2/TiO_2 heterostructure with remarkably enhanced hydrogen sorption properties through facile solvothermal approach, where 2D TiO_2 NS exhibit both nanoconfinement and catalytic effects. Surprisingly, we found that the oxygen vacancies were introduced into TiO_2 NS in the process of solvothermal treatment. Owing to the presence of oxygen vacancies and unique heterostructure, the obtained MgH_2/TiO_2 heterostructure exhibits impressive hydrogen storage performances with high stability and accelerated kinetics. Specifically, the $60MgH_2/TiO_2$ heterostructure presents low onset desorption temperature (180 °C) and superior long-term cycling stability with a capacity retention of 98.5% after 100 cycles at 300 °C, remarkably higher than that of the state-of-the-art TiO_2 catalyzed MgH_2 systems.

2 Experimental Section

2.1 Synthesis of MgH_2/TiO_2 Heterostructure

2.1.1 Synthesis of Graphene-like 2D TiO_2 Nanosheets

TiO_2 nanosheets were synthesized by a surfactant self-assembly method [34]. Firstly, 1.48 mL titanium isopropoxide (TTIP, 99.9%, Macklin) was added to 2.1 mL concentrated HCl under vigorous stirring (solution A). Meanwhile, 0.4 g poly(ethylene oxide)-block-poly(propylene oxide)-block-poly(ethylene oxide) triblock copolymer (P123, Mn = 5,800) was dissolved in 8 mL ethanol (solution B) by ultrasonication. Afterward, solution B was added dropwise into solution A and kept stirring for 30 min at room temperature. Then, 5 mL of the above resultants with 40 mL ethylene glycol was then transferred into a 100 mL stainless steel autoclave and heated at 150 °C for 20 h. Finally, the products were centrifuged and washed with ethanol, followed by freeze-drying to obtain 2D TiO_2 NS. Moreover, to improve the crystallinity and remove the impurities in TiO_2 NS, the pristine TiO_2 NS were annealed at different temperatures (300, 400, and 500 °C) for 2 h in the air (denoted as TiO_2-T, T represents the annealing temperature).

2.1.2 Synthesis of the MgH_2/TiO_2 Heterostructure

MgH_2/TiO_2 heterostructure was prepared by a bottom-up solvothermal strategy of in situ growth of MgH_2 nanoparticles on TiO_2 substrates. *Di-n*-butyl-magnesium ($MgBu_2$, 1 M solution in hexane, Sigma-Aldrich) and cyclohexane (C_6H_{12}, 99.5%, extra Dry, Sigma-Aldrich) were used as received states without further treatment. As provided in Table S1, different loading capacities of MgH_2 on TiO_2 NS of 40, 50, 60, 70, and 80 wt% were synthesized by changing the ratio between $MgBu_2$ and TiO_2 NS, which were denoted as $40MgH_2/TiO_2$, $50MgH_2/TiO_2$, $60MgH_2/TiO_2$, $70MgH_2/TiO_2$, and $80MgH_2/TiO_2$, respectively. In a typical synthesis of $60MgH_2/TiO_2$, 30 mg as-prepared TiO_2-300 NS and 1.8 mL $MgBu_2$ were firstly dispersed in 40 mL cyclohexane

under sonication. The mixture was then transferred into a 100 mL custom-designed autoclave, filled with 4.5 MPa H_2 pressure, and heated at 200 °C for 12 h under vigorous magnetic stirring [19, 42]. Finally, the resultants (named 60MgH_2/TiO_2 heterostructure) were collected by centrifugation, washed with cyclohexane several times, and dried at 80 °C overnight under dynamic vacuum. Moreover, blank MgH_2 without TiO_2 NS were also prepared under the same conditions for comparison.

2.2 Characterization and Measurements

The phase composition was characterized by using X-ray diffraction (XRD, Mini Flex 600) with Cu K_α radiation operated at 40 kV and 15 mA. The samples were prepared in an argon-filled glovebox and sealed in a custom-designed holder covered by the Scotch tape to avoid the possible oxidation during the XRD tests. The microstructure and morphological analyses were performed by scanning electron microscope (SEM, MIRA3 LHM) and transmission electron microscope (TEM, FEI Talos F200X G2). For TEM observations, the preparation of samples was carried out in the glovebox. The samples were dispersed in cyclohexane, sonicated, dropped on a copper grid, and rapidly transferred to the equipment. The preparation conditions of samples for SEM tests were similar to those for the TEM observation, except that the samples were dispersed in cyclohexane and dropped onto the silicon wafer. The in situ high-resolution transmission electron microscope (HRTEM) observation was applied to explore the microstructural evolution during the decomposition of the MgH_2/TiO_2 heterostructure under an irradiation beam current of 3 nA [43]. The valence state and chemical bonding nature of constituent elements of MgH_2/TiO_2 composites were analyzed by X-ray photoelectron spectroscopy (XPS, Kratos AXIS Ultra DLD). For XPS analyses, a special air-proof transfer vessel was used to transfer the samples from glovebox to the equipment. Electron paramagnetic resonance (EPR) measurement was performed at room temperature using a Bruker spectrometer (EMXplus-9.5/12). Solid-state ^1H magic-angle spinning nuclear magnetic resonance (MAS NMR) was carried out on a Bruker AVANCE NEO 600 spectrometer. Brunner–Emmet–Teller (BET) surface areas of all samples were measured by the N_2 isothermal ad/de-sorption tests at 77 K on Autosorb-IQ3 apparatus. Differential scanning calorimetry (DSC, NETZSCH STA 449 F3) measurements were performed at different heating rates (3, 5, and 10 °C min^{-1}) under a flowing Ar atmosphere to analyze the desorption kinetic properties. The DSC data were further processed by the Kissinger method to figure out the desorption apparent activation energy (E_a) according to the following equation:

$$\ln\left(\frac{\beta}{T_p^2}\right) = -\frac{E_a}{RT_p} + C \quad (1)$$

where β represents the heating rate, T_p refers to the peak temperature, R is the universal gas constant (R = 8.314 J mol^{-1} K^{-1}), and C is a constant.

The isothermal ab/de-sorption tests and temperature program desorption (TPD) measurements of samples were carried out by a Sievert-type pressure-composition-temperature apparatus (PCT, Shanghai Institute of Microsystem and Information Technology). For the isothermal ab/de-sorption tests, samples were loaded into the vessel in the glove box and were heated to the preset temperature at a heating rate of 10 °C min^{-1}. The initial hydrogen pressures for isothermal ab/de-sorption were 3 and 0.001 MPa, respectively. Besides, the hydrogenated samples were heated from room temperature to 350 °C with a heating rate of 2 °C min^{-1} to perform TPD measurements. The hydrogen pressure/duration/temperature parameters for cycling tests are set as 3 MPa/15 min/300 °C for re-hydrogenation and 0.001 MPa/15 min/300 °C for dehydrogenation. The hydrogen storage capacity was calculated in the weight percent of the entire composites including the TiO_2 scaffold.

3 Results and Discussion

3.1 Synthesis and Characterizations of the MgH_2/TiO_2 Heterostructure

The preparation procedure of the MgH_2/TiO_2 heterostructures is schematically illustrated in Scheme 1, including the synthesis of 2D TiO_2 NS and subsequent impregnation of $MgBu_2$ as well as the bottom-up self-assembly of MgH_2 nanoparticles anchored on TiO_2 NS. In a typical surfactant self-assembly synthesis process of TiO_2 NS, P123 and ethylene glycol (EG) acted as co-surfactants which played the role of structure-directing agents to form inverse lamellar micelles. The precursor oligomers (TTIP) were then self-assembled

 https://doi.org/10.1007/s40820-022-00891-9

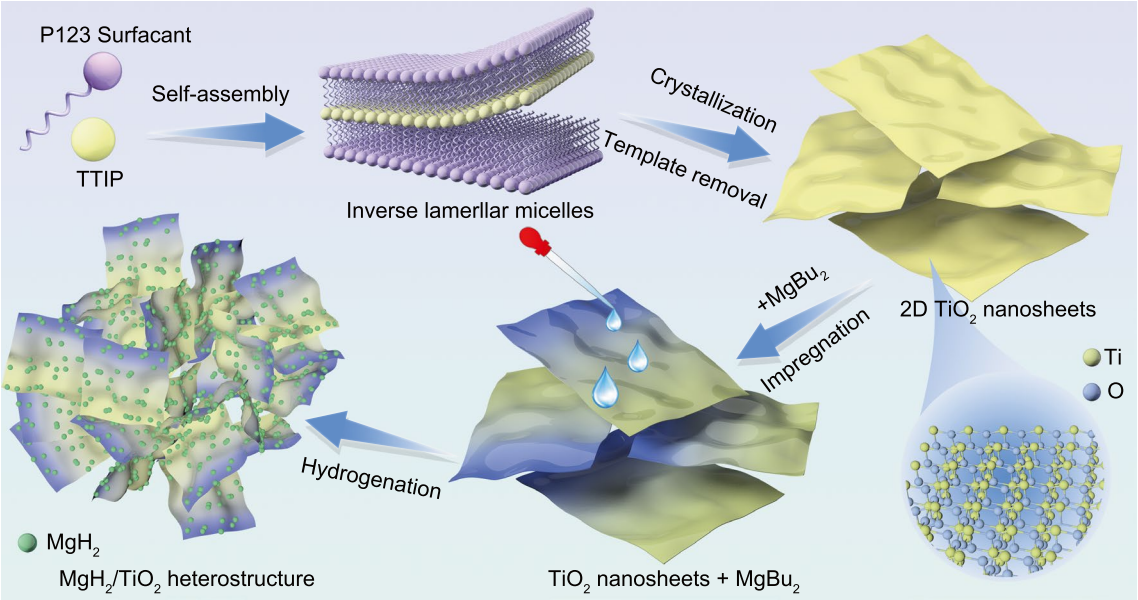

Scheme 1 Synthesis process illustration of the MgH_2/TiO_2 heterostructure

into lamellar structures with surfactant molecules, inducing the formation of layered inorganic oligomer agglomerates. Afterward, solvothermal treatment was carried out to promote the organization and crystallization of 2D TiO_2 NS. Subsequently, the TiO_2 NS were ultrasonically dispersed into the C_6H_{12} solution followed by the dropwise addition of $MgBu_2$. Finally, the MgH_2/TiO_2 heterostructure was obtained in the above dispersed suspension by hydrogenation of $MgBu_2$ on TiO_2 NS through a facile solvothermal method.

The typical morphology and structural features of the ultrathin 2D TiO_2 NS were observed using SEM and TEM. As shown in Fig. 1a–c, the pristine TiO_2 NS exhibit a morphology of 2D corrugated ultrathin nanosheets with their edges roll up owing to the surface tension, which is also observed in graphene as a general phenomenon. The sizes of the TiO_2 NS vary from 150 to 200 nm as seen from the TEM images. The thickness of the prepared TiO_2 NS was further characterized using AFM and TEM (Fig. S1). The obtained TiO_2 NS have a thickness of around 3.7 nm, corresponding to 5–6 monolayers, which confirms the formation of ultrathin nanosheets. In addition, the sheet-like structure of TiO_2 can be clearly distinguished in the HAADF and BF images (Fig. 1d), which may play a morphology-directing role in the solution-phase synthesis of nanostructured MgH_2. The EDS elemental mapping images demonstrate the homogeneous distribution of Ti and O elements (Fig. 1d).

Furthermore, the influence of the annealing temperature on the morphology of TiO_2 NS was also taken into account (Fig. S2). It is worth emphasizing that TiO_2-300 and TiO_2-400 exhibit a similar sheet-like structure as the pristine TiO_2 NS, except for the slight granulation after annealing at 400 °C. However, the crystallite size and crystallinity of TiO_2-500 increase obviously and the 2D nanostructures can hardly be observed. This phenomenon coincides well with the previous report [44]. Moreover, we also explored the stability of TiO_2 NS in the hydrogen atmosphere and it can be seen that the sheet-like structure of TiO_2 is still preserved after treatment in H_2 at 300 °C for 2 h (Fig. S2). Figure 1e shows the XRD patterns of pristine TiO_2, TiO_2-300, TiO_2-400, and TiO_2-500. According to the XRD patterns, pristine TiO_2 NS are mainly composed of the anatase phase (JCPDS No. 21–1272), as well as a small amount of rutile phase (JCPDS No. 21–1276). After calcination treatment, the intensities of the diffraction peaks are much sharper and stronger, manifesting an increase in crystallinity, coinciding well with the SEM and TEM results (Fig. S2). Additionally, the diffraction peaks of rutile phase disappear and crystalline diffraction peaks assigned to anatase TiO_2 crystal can be identified when the annealing temperature increases up to 400 and 500 °C. The specific surface area

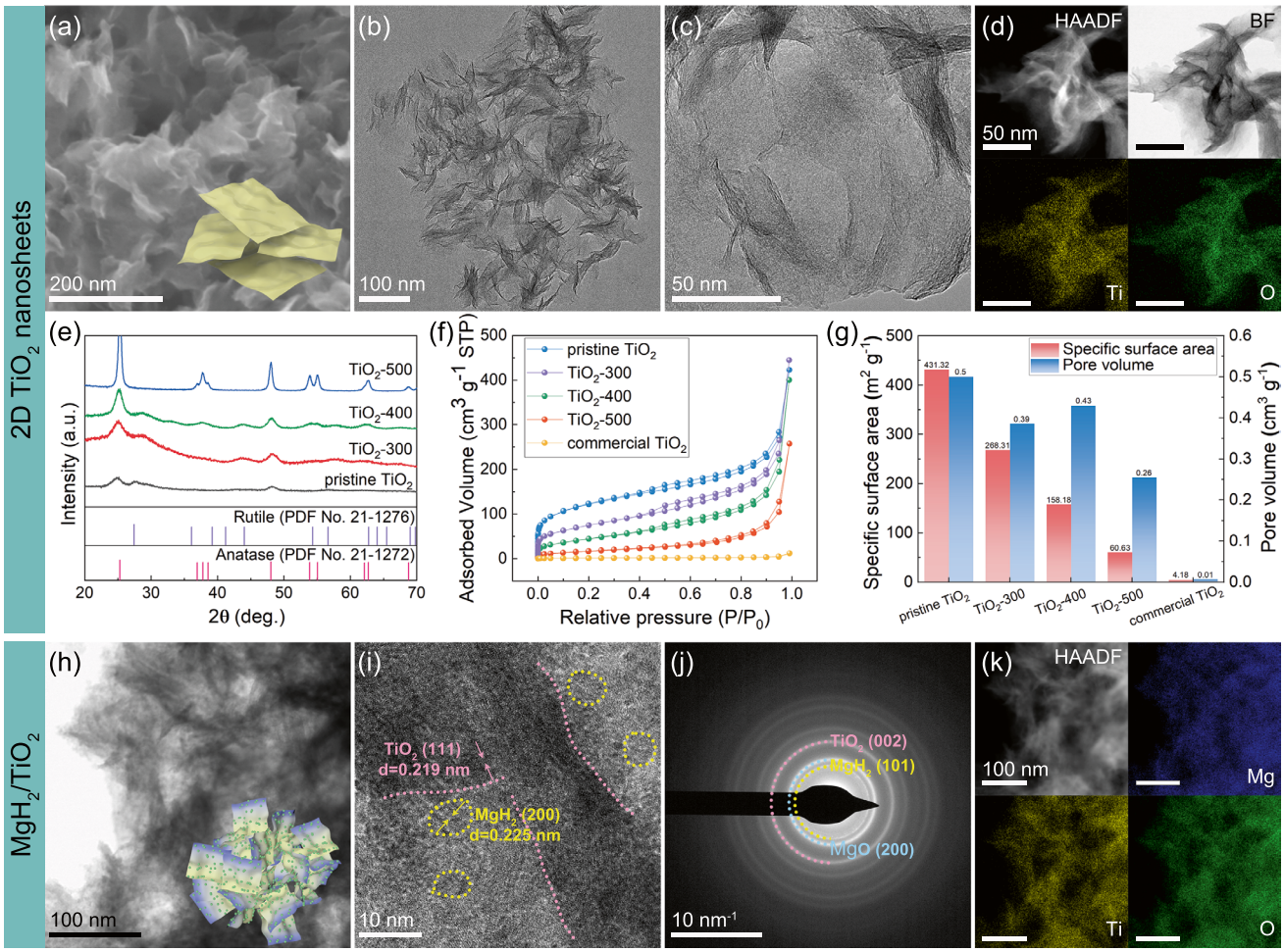

Fig. 1 **a** Typical SEM image of TiO_2 NS. **b, c** Typical TEM images at different scales. **d** Representative HAADF and BF images of TiO_2 NS as well as corresponding EDS elemental mapping results. **e** XRD patterns of TiO_2 NS. **f, g** N_2 ad/de-sorption isotherms and corresponding specific surface areas and pore-size distribution of pristine TiO_2 NS, commercial TiO_2, and TiO_2 NS treated at different annealing temperatures. **h-j** BF, HRTEM, and SAED images of as-synthesized $60MgH_2/TiO_2$ heterostructure. **k** HAADF images of as-synthesized $60MgH_2/TiO_2$ heterostructure and corresponding EDS elemental mapping results

and pore size distribution of TiO_2 NS were further investigated (Fig. 1f–g). Compared with commercial TiO_2, the specific surface area of TiO_2 NS is increased by 14–100 times, attributed to the special 2D sheet-like structures. The TiO_2 NS possess a specific surface area of 431.32 $m^2\ g^{-1}$, which is almost 100 times higher than that of the commercial TiO_2 (~4 $m^2\ g^{-1}$). Besides, it still possesses a high specific surface area of 268.31 $m^2\ g^{-1}$ even after calcination treatment (300 °C). Thus, we selected TiO_2-300 as the substrates to fabricate the MgH_2/TiO_2 heterostructure, and the TiO_2 mentioned below all refers to TiO_2-300 unless otherwise specified. The TiO_2 NS with ultrahigh specific surface area will provide more nucleation sites for nanoparticles, which could be ingeniously employed as the excellent scaffold for the self-assembly of MgH_2 NPs.

To fabricate MgH_2/TiO_2 heterostructure, $MgBu_2$ was used as the precursor and added into TiO_2 suspension followed by the solvothermal method under 4.5 MPa of hydrogen pressure. Impressively, the color of TiO_2 suspension fortuitously changed from white to dark blue with the addition of $MgBu_2$. The obvious blue color indicates the presence of oxygen vacancies caused by $MgBu_2$ [39], which will be discussed in detail in the following section. Figure 1h shows the typical TEM images of as-synthesized $60MgH_2/TiO_2$ heterostructure. It can be seen that TiO_2 nanosheets still maintain a graphene-like structure after the self-assembly of MgH_2

 https://doi.org/10.1007/s40820-022-00891-9

nanoparticles on them. Besides, 2D TiO_2 nanosheets are automatically arranged into flower-like structures to support and encapsulate MgH_2 nanoparticles, tremendously restricting the agglomeration of MgH_2 NPs and simultaneously hampering the re-stacking of TiO_2 NS in turn. According to the measurement of lattice spacing in HRTEM images (Fig. 1i), the interplanar spacings of 0.225 and 0.219 nm could be attributed to the (200) plane of MgH_2 (JCPDS No. 12–0697) and (111) plane of TiO_2 (JCPDS No. 21–1276), respectively. In addition, the diffraction rings in SAED pattern of $60MgH_2/TiO_2$ (Fig. 1j) reveal the formation of polycrystalline structure. Furthermore, the 2D wrinkled sheet-like structure of TiO_2 could be well distinguished from the HAADF images. EDS elemental mapping images confirm the homogeneous distribution of Mg, Ti, and O elements in the MgH_2/TiO_2 heterostructure (Fig. 1k).

3.2 Improved Hydrogen Storage Properties of the MgH_2/TiO_2 Heterostructure

The hydrogen storage performances of the MgH_2/TiO_2 heterostructure were further examined. Figure 2a shows the TPD profiles of blank MgH_2 and the MgH_2/TiO_2 with different loading of MgH_2 and Fig. 2b shows the comparison of the onset desorption temperature and hydrogen capacity of different samples. As the control sample, the blank MgH_2 starts to desorb hydrogen at about 295 °C, which is higher than those of MgH_2/TiO_2 composites, indicating that the TiO_2 NS indeed have a positive effect on the dehydrogenation of MgH_2. Concerning the MgH_2/TiO_2 with different loading capacities of MgH_2, the onset desorption temperatures decrease in the sequence of $50MgH_2/TiO_2$ (260 °C), $70MgH_2/TiO_2$ (233 °C), and $60MgH_2/TiO_2$ (200 °C). Thus, we further explored the hydrogen storage performances of $60MgH_2/TiO_2$, and the MgH_2/TiO_2 heterostructure mentioned below refers to the $60MgH_2/TiO_2$ unless otherwise specified. In the first non-isothermal desorption process, the $60MgH_2/TiO_2$ exhibits the initial desorption temperature of 200 °C with a total hydrogen release of 4 wt%. Notably, the $60MgH_2/TiO_2$ composite possesses a lower onset desorption temperature of 180 °C along with a hydrogen capacity of 3.4 wt% in the second non-isothermal dehydrogenation process. The lower desorption temperature in the second cycle reveals that the catalytic activity of TiO_2 NS varies upon de/ab-sorption behavior. The capacity loss after the first desorption may be attributed to the irreversible reaction between MgH_2 and TiO_2. It is therefore reasonable to speculate that the chemical environment of MgH_2 and TiO_2 in the first dehydrogenated sample should be considerably different from the as-synthesized sample, indicating the formation of catalytic species during initial hydrogen cycling, which is similar to what shown in previous reports [45–48], and will be discussed in later sections. In addition, DSC profiles (Figs. 2c and S3) show that the peak desorption temperature of commercial MgH_2 is 408.6 °C under the heating rate of 3 °C min^{-1}, while it tremendously reduces to 220.2 °C for the $60MgH_2/TiO_2$ heterostructure. According to the fitting results of DSC by Kissinger's equation, the apparent activation energy of $60MgH_2/TiO_2$ is determined to be 106.7 kJ mol^{-1} H_2, much lower than that of the commercial MgH_2 (142.27 kJ mol^{-1} H_2).

In order to further explore the influence of TiO_2 NS on MgH_2, the isotherm de/ab-sorption measurements were carried out for the $60MgH_2/TiO_2$ heterostructure as well as control samples (blank MgH_2 and commercial MgH_2). Figure 2d shows the isotherm desorption curves of the $60MgH_2/TiO_2$. As can been seen, the $60MgH_2/TiO_2$ releases hydrogen of 0.51, 1.56, 2.14, 2.83, and 2.43 wt% at the temperature of 180, 200, 250, 275, and 300 °C within 10 min, respectively. Moreover, even at a lower temperature of 180 °C, the composite can still desorb 1.24 wt% of hydrogen within 60 min, corresponding to 41% of the maximum hydrogen storage capacity. At 250 °C, 2.14 wt% of hydrogen can be desorbed within 10 min, while no hydrogen desorption is detected for the blank MgH_2 and commercial MgH_2 under identical conditions (Fig. S4). In addition, blank MgH_2 needs 68 min to release 80% of its theoretical hydrogen capacity at 300 °C. In contrast, it takes only 1.8 min for the $60MgH_2/TiO_2$ composite to reach the identical reaction extent (Fig. 2e). Impressively, the initial desorption rate is increased by 35 times for the $60MgH_2/TiO_2$ (Fig. 2f) when compared to that of blank MgH_2. This demonstrates the remarkably improved hydrogen storage performances of MgH_2 through the introduction of TiO_2 NS.

The isothermal re-hydrogenation curves of samples are presented in Fig. 2g-i. The $60MgH_2/TiO_2$ could absorb hydrogen even at a temperature as low as 80 °C with a hydrogen capacity of 1.86 wt% within 60 min. Such a low hydrogenation temperature meets the target of working temperature set by DOE for light-duty vehicle applications [7]. A

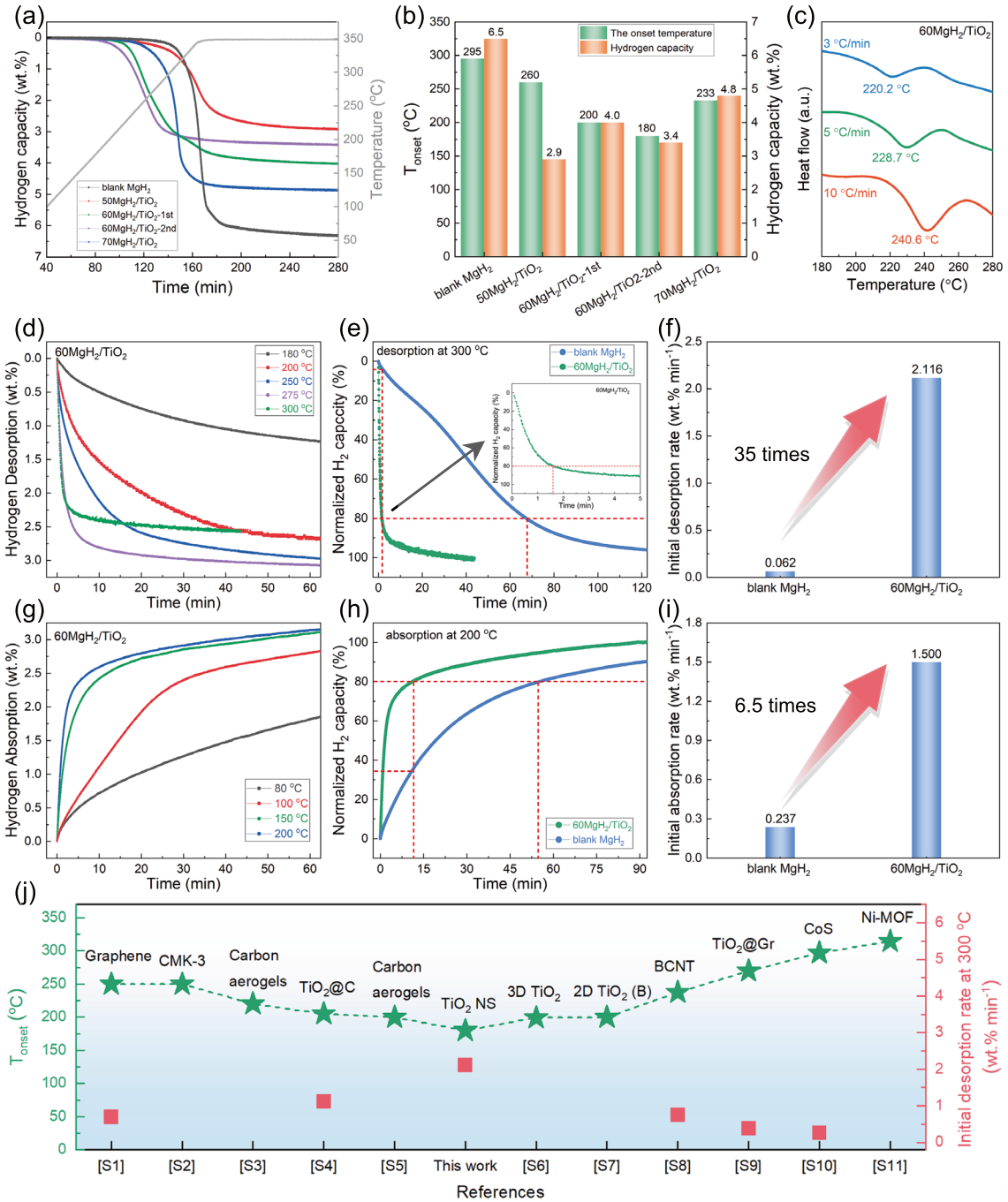

Fig. 2 **a, b** TPD curves and corresponding onset desorption temperature and hydrogen capacity of blank MgH_2, $50MgH_2/TiO_2$, $60MgH_2/TiO_2$-1st, $60MgH_2/TiO_2$-2nd, and $70MgH_2/TiO_2$. **c** DSC curves of $60MgH_2/TiO_2$. **d** Isothermal dehydrogenation profiles of $60MgH_2/TiO_2$. **e** Isothermal dehydrogenation curves and **f** initial desorption rate of $60MgH_2/TiO_2$ and blank MgH_2 at 300 °C. **g** Isothermal re-hydrogenation profiles of $60MgH_2/TiO_2$. **h** Isothermal re-hydrogenation curves and **i** initial absorption rate of $60MgH_2/TiO_2$ and blank MgH_2 at 200 °C. **j** Comparison of the onset desorption temperature and initial desorption rates at 300 °C of MgH_2/TiO_2 heterostructure with those of other nano-confined MgH_2 systems and TiO_2 catalyzed MgH_2 systems in the literature (Table S2)

hydrogen capacity of 2.65 wt%, corresponding to 80% of the maximum hydrogen capacity, is achieved at 200 °C within 11.9 min for the $60MgH_2/TiO_2$ heterostructure. However, it takes a long time of 54.8 min for the blank MgH_2 to achieve the same reaction extent (Fig. 2h). Additionally, it is noteworthy that the initial absorption rate of $60MgH_2/TiO_2$ at

https://doi.org/10.1007/s40820-022-00891-9

200 °C is 6.5 times that of the blank MgH_2 (Fig. 2i). The superior hydrogen desorption performances, such as high initial desorption rate and low desorption temperature of the $60MgH_2/TiO_2$, remarkably exceed those of the state-of-the-art MgH_2 systems reported in literature (Fig. 2j and Table S2).

Cycling stability is also a key factor for the practical application of hydrogen storage materials. To further evaluate the stability of the $60MgH_2/TiO_2$, long-term (100 cycles) isothermal de/re-hydrogenation was tested at a relatively high temperature of 300 °C (Fig. 3a). It can be seen that MgH_2/TiO_2 shows negligible degradation of the capacity even after 100 cycles (from 2.71 to 2.67 wt%) and a capacity retention as high as 98.5% is achieved (Fig. 3b), which is highly comparable with and even surpasses those of the previously reported Mg-based hydrogen storage materials catalyzed by TiO_2 and other transition metal oxides. Additionally, compared to the first cycle, the MgH_2/TiO_2 heterostructure exhibits a faster initial desorption rate during the second cycle (Fig. S5), which is associated with the formation of the catalytic oxide mentioned above. Moreover, the MgH_2/TiO_2 heterostructure still maintains flower-like structures and shows no obvious agglomeration of MgH_2 and restacking of TiO_2 NS even after 100 cycles (Fig. 3c). However, with the absence of TiO_2 NS, blank MgH_2 exhibits severe growth and agglomeration after several de/re-hydrogenation cycles (Fig. S6). The high stability of the MgH_2/TiO_2 heterostructure is presumably ascribed to the confinement effect of 2D TiO_2 NS on MgH_2 and robust interfacial contact between host and support materials.

Therefore, the MgH_2/TiO_2 heterostructure exhibits rapid hydrogen ab/de-sorption kinetics and excellent long-term cycling stability than those of blank MgH_2, highlighting the crucial role of the 2D TiO_2 nanosheets, which simultaneously possess catalytic effect to MgH_2 and inhibit the agglomeration of MgH_2.

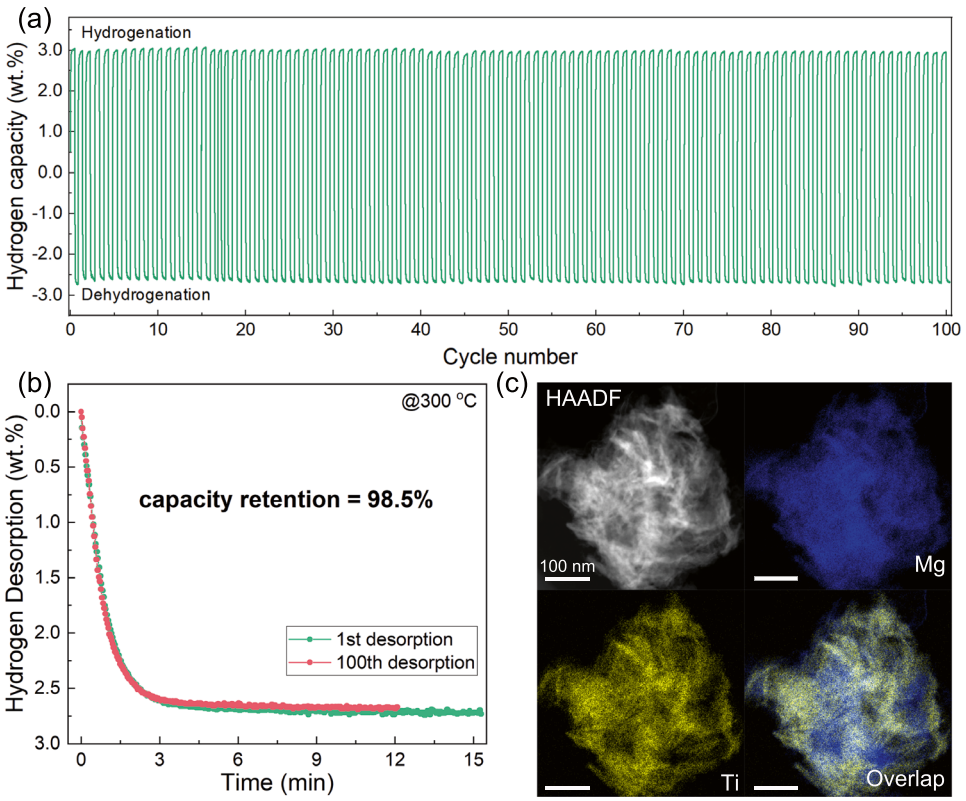

Fig. 3 **a** Reversible hydrogen absorption and desorption cycling profiles of $60MgH_2/TiO_2$ at 300 °C. **b** Hydrogen desorption curves of $60MgH_2/TiO_2$ at different cycles (1st and 100th). **c** HAADF images of $60MgH_2/TiO_2$ after 100 cycles and corresponding EDS elemental mapping results

3.3 Catalytic Mechanism of the MgH_2/TiO_2 Heterostructure

In order to further understand the mechanism of improved sorption performances of the MgH_2/TiO_2 heterostructure, we further characterized the phase components and microstructure of samples at different states. Figure 4 displays the optical photographs and microstructure of pristine TiO_2 NS and $MgBu_2$-treated TiO_2 NS. As shown in Fig. 4a, the $MgBu_2$-treated TiO_2 NS exhibit in different colors ranging from blue to black, in marked contrast with the white pristine TiO_2 powders. The color change of TiO_2 is ascribed to the presence of oxygen vacancies, which coincides well with the previous work [39–41, 49]. Herein, we introduce oxygen vacancies into TiO_2 NS by a facile strategy, that is, the impregnation of $MgBu_2$ into TiO_2 NS. We discover that the $MgBu_2$ could not only act as the reducing agent to fabricate oxygen vacancy-rich blue TiO_2 NS but also serve as the precursor of MgH_2 to promote the self-assembly of MgH_2 nanoparticles onto TiO_2 NS through subsequent solvothermal approaches. Such a "one-stone-two-birds" effect enables the MgH_2/TiO_2 heterostructure as a promising hydrogen storage material with superior performances. Figure 4b displays the identical crystalline structure with the anatase phase in the majority and that of rutile in minority for different TiO_2 samples, indicating that the impregnation of $MgBu_2$ does not destroy the intrinsic crystal structure of the TiO_2 nanosheets. Besides, XPS spectra of elemental Ti (Fig. 4c) and O (Fig. S7) are provided. The high-resolution XPS spectra of Ti 2*p* of the pristine TiO_2 NS and TiO_2-300 at 464.4 and 458.6 eV can be attributed to Ti^{4+} $2p_{1/2}$ and Ti^{4+} $2p_{3/2}$, respectively, while the peaks of TiO_2 NS treated with $MgBu_2$ slightly shift toward lower binding energy, indicating that Ti^{3+} is generated with the formation of oxygen vacancies. The O 1*s* peaks located at 531.8, 530.8, and 529.5 eV belong to adsorbed oxygen (O_A), oxygen vacancy (O_V), and lattice oxygen (O_L) in the $MgBu_2$-treated TiO_2 NS, respectively (Fig. S7). Based on the peak area of O_V to the overall peak area of O 1*s*, the percentage of O_V on the surface of the $MgBu_2$-treated TiO_2 is determined to be 32.53%. Additionally, the concentration

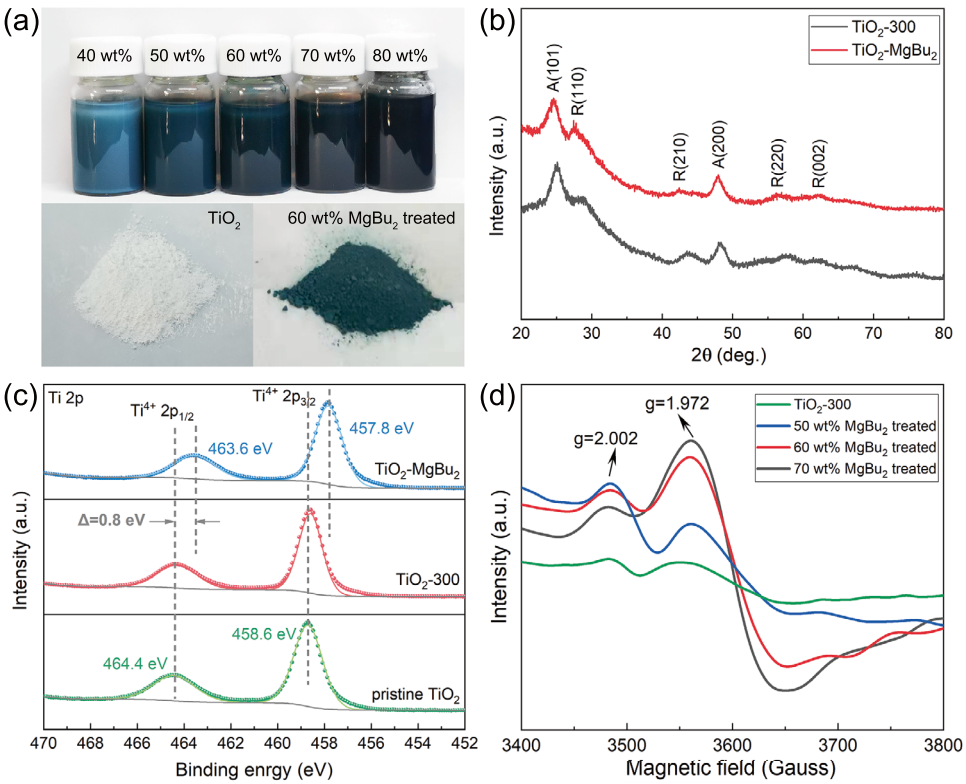

Fig. 4 **a** Optical photographs of TiO_2 NS suspension treated with different amounts of $MgBu_2$. **b** XRD patterns of TiO_2-300 and $MgBu_2$-treated TiO_2 NS. **c** High-resolution XPS spectra of Ti 2*p*. **d** EPR spectra of TiO_2-300 and TiO_2 NS treated with different amounts of $MgBu_2$ ("40wt%/ 50wt%/ 60wt%/ 70wt%/ 80wt% " refers to the weight percentage of MgH_2 in the MgH_2/TiO_2 heterostructure)

https://doi.org/10.1007/s40820-022-00891-9

of oxygen vacancies on the surface of the as-synthesized MgH_2/TiO_2 heterostructure (33.4%) shows no significant change when compared to that on the TiO_2 NS treated with $MgBu_2$ (Fig. S7).

Moreover, EPR measurement was carried out to further explore the existence of oxygen vacancies in TiO_2 NS treated with $MgBu_2$. As shown in Fig. 4d, the TiO_2 NS treated with $MgBu_2$ exhibit typical EPR signals at about $g = 1.972$ and $g = 2.002$, which could be attributed to Ti^{3+} and oxygen vacancies in the lattice, respectively [40, 50]. All these results strongly prove that the oxygen vacancies have been successfully introduced into TiO_2 nanosheets by the "one-stone-two-birds" strategy. Due to the higher electrical conductivity, numerous active sites, and enlarged lattice space derived from oxygen vacancies, the formation of oxygen vacancy-rich blue TiO_2 could not only accelerate the migration of electrons and diffusion of hydrogen atoms but also provide more active sites for the capture of hydrogen and nucleation of MgH_2/Mg. Thus, the MgH_2/TiO_2 heterostructure displays superior hydrogen ab/de-sorption kinetic properties.

In order to elucidate the catalytic mechanism, the structural stability of the MgH_2/TiO_2 composites during the hydrogen de/ab-sorption process was further investigated. Figure 5 shows the TEM images of dehydrogenated and re-hydrogenated $60MgH_2/TiO_2$ heterostructure. Surprisingly, there are no significant differences in morphology among the as-synthesized (Fig. 1h–k), dehydrogenated (Fig. 5a–d), and re-hydrogenated (Fig. 5e–h) samples, further confirming the thermal stability of the MgH_2/TiO_2 composites. Notably, by measuring the interplanar spacing of the well-resolved lattice fringes (Fig. 5b, f), we observe a new Mg-Ti ternary oxide, which is discussed in detail below. Thus, the establishment of the flower-like heterostructure has rendered the ability to well maintain the primary structure of the TiO_2 scaffold and MgH_2 nanoparticles, thereby improving the long-term cycling stability of MgH_2 and facilitating rapid transport of electrons and hydrogen.

We further explored the phase transformation and chemical valence state change of MgH_2/TiO_2 at different states. The XRD patterns of as-synthesized samples exhibit broad diffraction peaks indicating the presence of nano-sized MgH_2 (Fig. 6a). No peaks from MgO (which generally appear at the peak position of ~ 42.9° and 62.3° [11]) can be detected in the XRD pattern of as-synthesized MgH_2/TiO_2, indicating the absence of MgO. After dehydrogenation, in addition to the main phase of Mg, two new broad peaks located at 42.7° and 62.0° appear in the XRD patterns, which are close to the peak positions of MgO. In the subsequent hydrogen absorption process, Mg phase transforms to MgH_2 and those two characteristic peaks assigned to Mg_2TiO_4 (JCPDS No. 16–0215) show no obvious change. Additionally, as shown in Fig. S8, the phase composition of the MgH_2/TiO_2 heterostructure remains unchanged after 100 de/re-hydrogenation cycles by showing very similar XRD patterns. Such a Mg-Ti oxide phase may possess a catalytic effect for the de/re-hydrogenation of MgH_2 [45, 47]. As is well known, the existence of MgO will deteriorate the performance of MgH_2; hence, higher temperature is required for the release of hydrogen [51]. However, the MgH_2/TiO_2 composites perform excellent hydrogen desorption properties. To further prove that these two peaks belong to the highly catalytic Mg-Ti oxide instead of less-catalytic MgO, ^1H NMR test was conducted (Figs. 6b and S9). A shorter spin–lattice relaxation time of MgH_2/TiO_2 (~ 1.54 s) compared with that of blank MgH_2 (~ 4.50 s) indicates a faster H motion in MgH_2/TiO_2. In particular, the MgH_2/TiO_2 heterostructure exhibits a much shorter spin–lattice relaxation time of 1.49 s after the 1st re-hydrogenation than that of the as-synthesized MgH_2/TiO_2, indicating that new species with catalytic activity have formed during the first dehydrogenation process. Thus, it is demonstrated that two characteristic peaks centered at 42.7° and 62.0° are assigned to the ternary Mg-Ti oxide phase ($MgTi_2O_4$), having much higher catalytic activity than MgO. It can be deduced that the Mg-Ti oxide is formed by the chemical reaction at the interface between MgH_2 and TiO_2 NS during the first hydrogen desorption process. The similar phenomenon, for which Ti/Nb oxide could react with MgH_2 and result in the formation of a new ternary oxide, has also been reported in the previous work [48]. Compared to Mg/MgH_2, the broader diffraction peaks of the ternary Mg-Ti oxide phase manifest its smaller crystallite size than that of Mg/MgH_2.

To further clarify the role of the ternary Mg-Ti oxide in the dehydrogenation process, in situ HRTEM observations were carried out by real-time recording of the structure and composition evolution of hydrogenated MgH_2/TiO_2 during the hydrogen desorption process (Fig. 6c). Additional images with more details are shown in Fig. S10. Before electron beam irradiation (at 0 min), MgH_2 (101) and TiO_2 nanosheets could be identified according to the lattice fringe spacings. After irradiation under a beam current of 3 nA

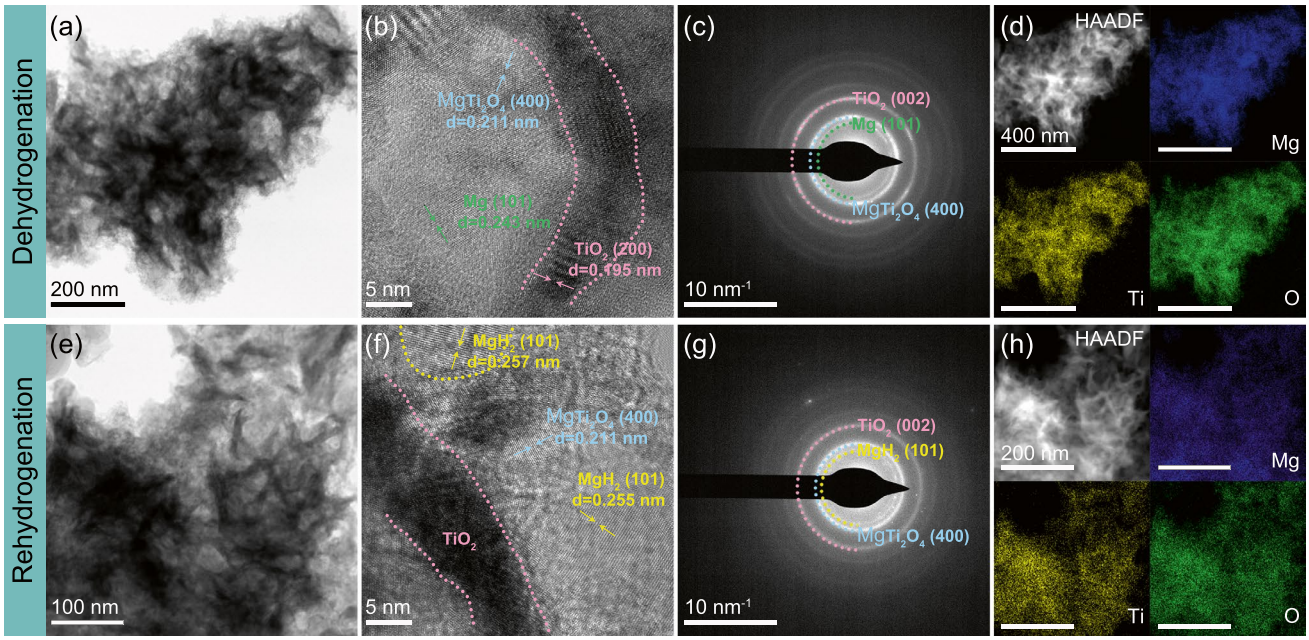

Fig. 5 BF, HRTEM, SAED, HAADF images as well as EDS elemental mapping results of dehydrogenated **a-d** and re-hydrogenated **e–h** $60MgH_2/TiO_2$ heterostructure

for 1.5 min, a portion of MgH_2 react with TiO_2, generating a thin Mg-Ti oxide layer. After 2.5 min of irradiation, the MgH_2 near Mg-Ti oxide begins to release hydrogen to form Mg. The observed area releases hydrogen completely after 3 min. It can be seen that, unlike the neat MgO layer, the in-built ternary Mg-Ti oxide catalyst could act as a pathway to facilitate hydrogen diffusion, resulting in improved reaction kinetics. Through the pathways provided by Mg-Ti oxide, the hydrogen can diffuse into/out of Mg/MgH_2, possibly by a formation of metastable titanium hydride (TiH_x) species [19, 52], which coincides well with the XPS chemical state shifts discussed later. In addition, Mg-Ti oxide at the MgH_2/TiO_2 interfaces could also strongly anchor MgH_2 nanoparticles, which significantly inhibits the growth and agglomeration of MgH_2 particles during cycling. Moreover, the high ductility and flexibility of the Mg-Ti oxide [53] can significantly buffer the volume change of MgH_2 particles during de/re-hydrogenation cycles, preventing the detachment of MgH_2 from the TiO_2 substrate and thereby ensuring the excellent cyclic stability.

Moreover, XPS analyses were employed to explore the evolution of the bonding state of Ti in the process of de/re-hydrogenation and the results are shown in Fig. 6d. XPS survey spectrum indicates the coexistence of Mg, O, and Ti elements (Fig. S11), well coincident with the EDS mapping results. As shown in the high-resolution Ti 2*p* XPS spectra, the signals of Ti^{4+} species (458.8 eV for $2p_{3/2}$ and 464.5 eV for $2p_{1/2}$) can be detected in all samples at different states, indicating that TiO_2 nanosheets still exist in the MgH_2/TiO_2 heterostructure during hydrogen ab/de-sorption process. Additionally, the typical doublets located at 456.8 and 462.5 eV of Ti^{3+} for as-synthesized MgH_2/TiO_2 composites further confirm the successful introduction of oxygen vacancies. Moreover, it can be seen that the Ti 2*p* signals of Ti^{2+} appear in the dehydrogenated samples and Ti^{2+} peaks shift to higher binding energies in the re-hydrogenated samples. The presence of Ti^{2+} peaks testifies the formation of low-valence Ti-H active species. The slight change of the peak position of Ti^{2+} demonstrates that Ti-H active species could act as the intermediates to promote the transportation of electrons and hydrogen [19], further proving that the Mg-Ti oxide acts as a pathway to promote hydrogen diffusion. It is well known that the electronegativity of Ti (1.54) is between Mg (1.31) and H (2.2) [21, 54]. Variable valence of Ti could also facilitate the electron transfer between Mg^{2+} and H^-, providing a favorable condition for weakening the Mg-H bond. In addition, numerous multi-phase interfaces composed of MgH_2 and multivalence Ti promote the diffusion

 https://doi.org/10.1007/s40820-022-00891-9

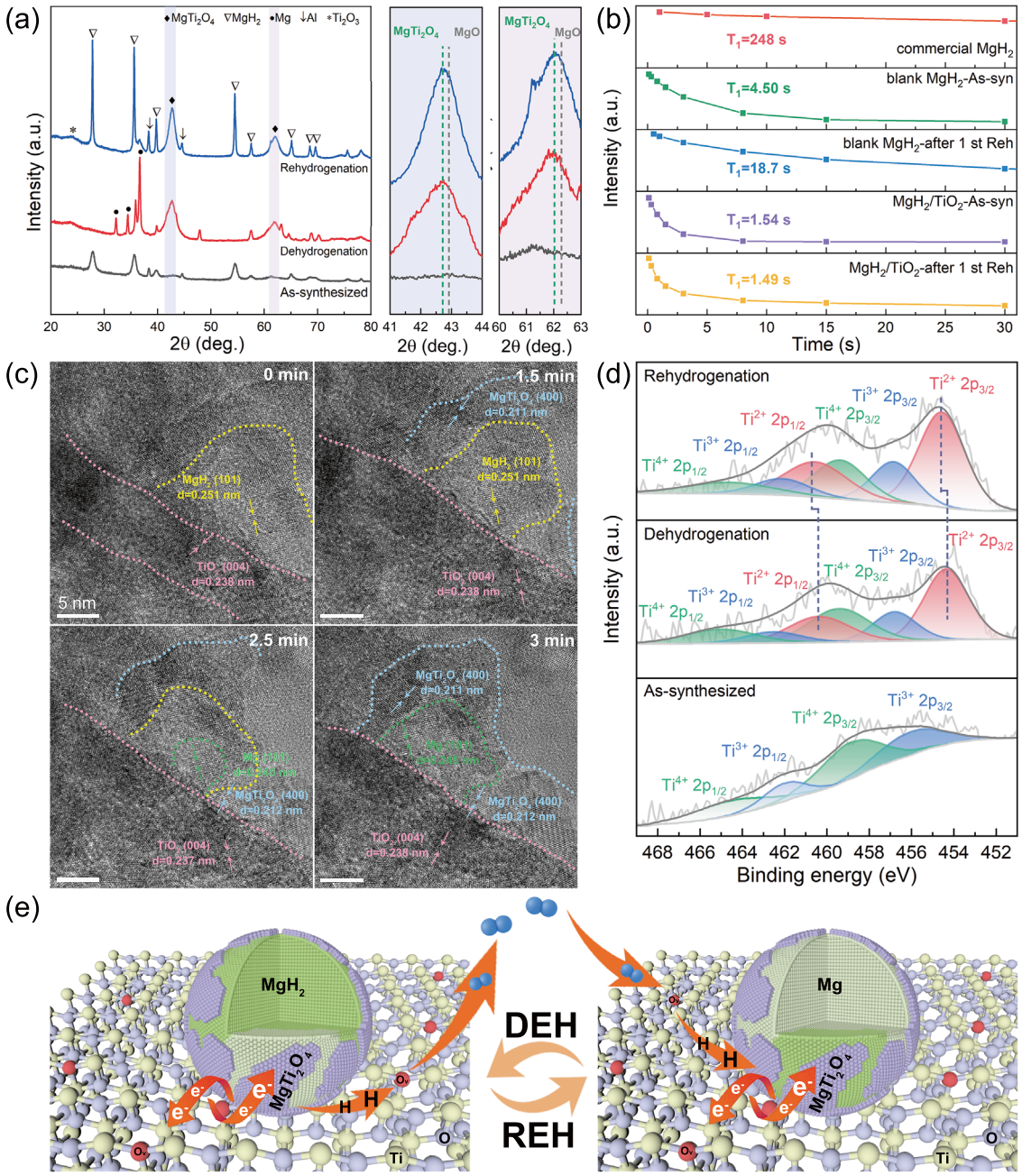

Fig. 6 **a** XRD patterns of the as-synthesized, dehydrogenated, and re-hydrogenated 60MgH_2/TiO_2 heterostructure. **b** NMR spin lattice relaxation times of 60MgH_2/TiO_2, commercial MgH_2, and blank MgH_2. **c** In situ HRTEM images showing the microstructure evolution of the hydrogenated 60MgH_2/TiO_2 during the hydrogen desorption process. **d** High-resolution Ti 2*p* spectra of 60MgH_2/TiO_2 at different states. **e** Schematic diagram showing the hydrogenation and dehydrogenation mechanisms of MgH_2/TiO_2 heterostructure

of hydrogen and electron and provide more nucleation sites for MgH_2/Mg. Thus, the existence of multivalence Ti-based catalysts accounts for the significantly enhanced hydrogen storage performances of the MgH_2/TiO_2 heterostructure.

Based on the experimental results and analyses, it is concluded that the superior hydrogen storage performances of the MgH_2/TiO_2 heterostructure can be attributed to the intrinsic and extrinsic synergistic effects, as illustrated in Fig. 6e: (1) Graphene-like 2D TiO_2 nanosheets with a high

specific surface area provide the unimpeded channels for the rapid diffusion of hydrogen and more nucleation sites for MgH_2/Mg, thereby improving the kinetics of de/re-hydrogenation. (2) Nano-sized MgH_2 are uniformly confined on TiO_2 nanosheets to form a flower-like heterostructure, which significantly suppresses the growth and agglomeration of MgH_2 during the hydrogen ab/de-sorption processes, ensuring the excellent cycling stability. Meanwhile, the re-stacking of TiO_2 nanosheets can be hampered in turn. (3) Abundant oxygen vacancies introduced by the "one-stone-two-birds" strategy significantly enhance the electrical conductivity of TiO_2 NS and provide additional active sites for transportation of electrons and hydrogen, leading to greatly enhanced hydrogen sorption kinetics. (4) The ternary Mg-Ti oxide catalyst located at the interface of MgH_2 and TiO_2 acts as the pathway to facilitate hydrogen diffusion, resulting in improved hydrogen storage properties. In addition, Mg-Ti oxide possesses better ductility and flexibility than pure MgO. Thus, due to the stable interfacial bonding strength between oxide layers and the MgH_2 nanoparticles, Mg-Ti oxide may exhibit a long-term confinement effect on MgH_2 nanoparticles and significantly buffer successive expansion and contraction of MgH_2 particles during de/re-hydrogenation cycles, improving reversible cycling performance. (5) Multi-valence Ti-based catalysts favor the electron transfer between Mg^{2+} and H^-, weakening the Mg-H bond. Additionally, numerous multi-phase interfaces composed of Mg^{2+} and multi-valence Ti containing species could provide more diffusion pathways for hydrogen and more nucleation sites for MgH_2/Mg.

4 Conclusion

In the present work, a flower-like MgH_2/TiO_2 heterostructure has been successfully synthesized using oxygen vacancy-rich 2D TiO_2 NS as the functional scaffold. Benefitting from the intrinsic (nano-sized MgH_2) and extrinsic (catalytic activity of Mg-Ti oxide at interfaces) effects as well as the incorporation of oxygen vacancies, the prepared MgH_2/TiO_2 heterostructure exhibits superior hydrogen storage performances. Specifically, the composite shows excellent desorption performances with a low onset desorption temperature down to 180 °C and a rapid initial dehydrogenation rate at 300 °C (2.116 wt% min^{-1}), surpassing those of the state-of-the-art MgH_2 systems catalyzed by TiO_2. Meanwhile, the MgH_2/TiO_2 heterostructure displays an excellent cycling stability with a capacity retention of 98.5% after 100 cycles at 300 °C. This work offers a promising approach for applying graphene analogues to the construction of advanced hydrogen storage materials with 0D/2D heterostructures.

Acknowledgements We would like to thank the support from the National Natural Science Foundation (No. 52171186), the Science and Technology Commission of Shanghai Municipality under No. 19511108100, Shanghai Education Commission "Shuguang" scholar Project (16SG08). The authors also appreciate the financial support from the Center of Hydrogen Science, Shanghai Jiao Tong University.

Funding Open access funding provided by Shanghai Jiao Tong University.

Supplementary Information The online version contains supplementary material available at https://doi.org/10.1007/s40820-022-00891-9.

References

1. L. Schlapbach, A. Zuttel, Hydrogen-storage materials for mobile applications. Nature **414**(6861), 353–358 (2001). https://doi.org/10.1038/35104634
2. D. Pukazhselvan, V. Kumar, S.K. Singh, High capacity hydrogen storage: basic aspects, new developments and milestones. Nano Energy **1**(4), 566–589 (2012). https://doi.org/10.1016/j.nanoen.2012.05.004
3. P. Nicola, M. Andrea, M. Vittorio, P. Luca, Interfaces within biphasic nanoparticles give a boost to magnesium-based hydrogen storage. Nano Energy **72**, 104654 (2020). https://doi.org/10.1016/j.nanoen.2020.104654
4. X. Yu, Z. Tang, D. Sun, L. Ouyang, M. Zhu, Recent advances and remaining challenges of nanostructured materials for hydrogen storage applications. Prog. Mater. Sci. **88**, 1–48 (2017). https://doi.org/10.1016/j.pmatsci.2017.03.001

5. N.M. Dowell, N. Sunny, N. Brandon, H. Herzog, A.Y. Ku et al., The hydrogen economy: a pragmatic path forward. Joule **5**(10), 2524–2529 (2021). https://doi.org/10.1016/j.joule.2021.09.014
6. M. Spek, C. Banet, C. Bauer, P. Gabrielli, W. Goldthorpe et al., Perspective on the hydrogen economy as a pathway to reach net-zero CO_2 emissions in Europe. Energy Environ. Sci. **15**(3), 1034–1077 (2022). https://doi.org/10.1039/D1EE02118D
7. C. Weidenthaler, M. Felderhoff, Solid-state hydrogen storage for mobile applications: Quo Vadis? Energy Environ. Sci. **4**(7), 2495–2502 (2011). https://doi.org/10.1039/c0ee00771d
8. H. Shao, G. Xin, J. Zheng, X. Li, E. Akiba, Nanotechnology in Mg-based materials for hydrogen storage. Nano Energy **1**(4), 590–601 (2012). https://doi.org/10.1016/j.nanoen.2012.05.005
9. P. Larsson, C.M. Araujo, J.A. Larsson, P. Jena, R. Ahuja, Role of catalysts in dehydrogenation of MgH_2 nanoclusters. PNAS **105**, 8227–8231 (2008). https://doi.org/10.1073/.0711743105
10. M. Liu, X. Xiao, S. Zhao, M. Chen, J. Mao et al., Facile synthesis of Co/Pd supported by few-walled carbon nanotubes as an efficient bidirectional catalyst for improving the low temperature hydrogen storage properties of magnesium hydride. J. Mater. Chem. A **7**(10), 5277–5287 (2019). https://doi.org/10.1039/C8TA12431K
11. K. Xian, M. Wu, M. Gao, S. Wang, Z. Li et al., A unique nanoflake-shape bimetallic Ti–Nb oxide of superior catalytic effect for hydrogen storage of MgH_2. Small (2022). https://doi.org/10.1002/smll.202107013
12. X. Lu, L. Zhang, H. Yu, Z. Lu, J. He et al., Achieving superior hydrogen storage properties of MgH_2 by the effect of TiFe and carbon nanotubes. Chem. Eng. J. **422**, 130101 (2021). https://doi.org/10.1016/j.cej.2021.130101
13. Z. Lan, H. Fu, R. Zhao, H. Liu, W. Zhou et al., Roles of in situ-formed NbN and Nb_2O_5 from N-doped Nb_2C MXene in regulating the re/hydrogenation and cycling performance of magnesium hydride. Chem. Eng. J. **431**, 133985 (2022). https://doi.org/10.1016/j.cej.2021.133985
14. J. Mao, T. Huang, S. Panda, J. Zou, W. Ding, Direct observations of diffusion controlled microstructure transition in Mg-In/Mg-Ag ultrafine particles with enhanced hydrogen storage and hydrolysis properties. Chem. Eng. J. **418**, 129301 (2021). https://doi.org/10.1016/j.cej.2021.129301
15. X. Ding, R. Chen, X. Chen, H. Fang, Q. Wang et al., A novel method towards improving the hydrogen storage properties of hypoeutectic Mg-Ni alloy via ultrasonic treatment. J. Magnes. Alloy. (2021). https://doi.org/10.1016/j.jma.2021.06.003
16. F. Guo, T. Zhang, L. Shi, L. Song, Hydrogen absorption/desorption cycling performance of Mg-based alloys with in-situ formed Mg_2Ni and LaH_x (x = 2, 3) nanocrystallines. J. Magnes. Alloy. (2021). https://doi.org/10.1016/j.jma.2021.06.013
17. K.J. Jeon, H.R. Moon, A.M. Ruminski, B. Jiang, C. Kisielowski et al., Air-stable magnesium nanocomposites provide rapid and high-capacity hydrogen storage without using heavy-metal catalysts. Nat. Mater. **10**(4), 286–290 (2011). https://doi.org/10.1038/nmat2978
18. M. Liu, S. Zhao, X. Xiao, M. Chen, C. Sun et al., Novel 1D carbon nanotubes uniformly wrapped nanoscale MgH_2 for efficient hydrogen storage cycling performances with extreme high gravimetric and volumetric capacities. Nano Energy **61**, 540–549 (2019). https://doi.org/10.1016/j.nanoen.2019.04.094
19. W. Zhu, L. Ren, C. Lu, H. Xu, F. Sun et al., Nanoconfined and in situ catalyzed MgH_2 self-assembled on 3D Ti_3C_2 MXene folded nanosheets with enhanced hydrogen sorption performances. ACS Nano **15**(11), 18494–18504 (2021). https://doi.org/10.1021/acsnano.1c08343
20. C. Lu, J. Zou, X. Zeng, W. Ding, Hydrogen storage properties of core-shell structured Mg@TM (TM = Co, V) composites. Int. J. Hydrog. Energy **42**(22), 15246–15255 (2017). https://doi.org/10.1016/j.ijhydene.2017.04.063
21. J. Cui, J. Liu, H. Wang, L. Ouyang, D. Sun et al., Mg-TM (TM: Ti, Nb, V Co, Mo or Ni) core-shell like nanostructures: synthesis, hydrogen storage performance and catalytic mechanism. J. Mater. Chem. A **2**(25), 9645–9655 (2014). https://doi.org/10.1039/c4ta00221k
22. K. Wang, X. Zhang, Y. Liu, Z. Ren, X. Zhang et al., Graphene-induced growth of N-doped niobium pentaoxide nanorods with high catalytic activity for hydrogen storage in MgH_2. Chem. Eng. J. **406**, 126831 (2021). https://doi.org/10.1016/j.cej.2020.126831
23. S. Milošević, S. Kurko, L. Pasquini, L. Matović, R. Vujasin et al., Fast hydrogen sorption from MgH_2-VO_2(B) composite materials. J. Power Sources **307**, 481–488 (2016). https://doi.org/10.1016/j.jpowsour.2015.12.108
24. K. Wang, X. Zhang, Z. Ren, X. Zhang, J. Hu et al., Nitrogen-stimulated superior catalytic activity of niobium oxide for fast full hydrogenation of magnesium at ambient temperature. Energy Stor. Mater. **23**, 79–87 (2019). https://doi.org/10.1016/j.ensm.2019.05.029
25. Q. Zhang, Y. Wang, L. Zang, X. Chang, L. Jiao et al., Core-shell Ni_3N@Nitrogen-doped carbon: synthesis and application in MgH_2. J. Alloys Compd. **703**, 381–388 (2017). https://doi.org/10.1016/j.jallcom.2017.01.224
26. C. Jie, W. Hui, L. Jiangwen, O. Liuzhang, Z. Qingan et al., Remarkable enhancement in dehydrogenation of MgH_2 by a nano-coating of multi-valence Ti-based catalysts. J. Mater. Chem. A **1**(18), 5603–5611 (2013). https://doi.org/10.1039/c3ta01332d
27. J. Ankur, A. Shivani, K. Sanjay, Y. Shotaro, M. Hiroki et al., How does TiF_4 affect the decomposition of MgH_2 and its complex variants? - an XPS investigation. J. Mater. Chem. A **5**(30), 15543 (2017). https://doi.org/10.1039/c7ta03081a
28. Y. Zhang, X. Zhuang, Y. Zhu, N. Wan, L. Li et al., Synergistic effects of TiH_2 and Pd on hydrogen desorption performances of MgH_2. Int. J. Hydrog. Energy **40**(46), 16338–16346 (2015). https://doi.org/10.1016/j.ijhydene.2015.09.029
29. L. Mykhaylo, D. Roman, A.Y. Volodymyr, E. Jon, G. Jonathan et al., An outstanding effect of graphite in nano-MgH_2-TiH_2 on hydrogen storage performance. J. Mater. Chem. A **6**, 10740–10754 (2018). https://doi.org/10.1039/c8ta02969e
30. R.A. Pavel, C. Fermin, L. Michel, Hydrides of early transition metals as catalysts and grain growth inhibitors for enhanced reversible hydrogen storage in nanostructured magnesium. J. Mater. Chem. A **7**, 23064–23075 (2019). https://doi.org/10.1039/c9ta05440e

31. S.K. Verma, A. Bhatnagar, V. Shukla, P.K. Soni, A.P. Pandey et al., Multiple improvements of hydrogen sorption and their mechanism for MgH_2 catalyzed through TiH_2@Gr. Int. J. Hydrog. Energy **45**(38), 19516–19530 (2020). https://doi.org/10.1016/j.ijhydene.2020.05.031
32. K. Wang, G. Wu, H. Cao, H. Li, X. Zhao, Improved reversible dehydrogenation properties of MgH_2 by the synergetic effects of graphene oxide-based porous carbon and $TiCl_3$. Int. J. Hydrog. Energy **43**(15), 7440–7446 (2018). https://doi.org/10.1016/j.ijhydene.2018.02.195
33. G. Xia, Y. Tan, X. Chen, D. Sun, Z. Guo et al., Monodisperse magnesium hydride nanoparticles uniformly self-assembled on graphene. Adv. Mater. **27**(39), 5981–5988 (2015). https://doi.org/10.1002/adma.201502005
34. Z. Sun, T. Liao, Y. Dou, S.M. Hwang, M.S. Park et al., Generalized self-assembly of scalable two-dimensional transition metal oxide nanosheets. Nat. Commun. **5**, 3813 (2014). https://doi.org/10.1038/ncomms4813
35. X. Zhang, L. Hou, A. Ciesielski, P. Samorì, 2D materials beyond graphene for high-performance energy storage applications. Adv. Energy Mater. **6**(23), 1600671 (2016). https://doi.org/10.1002/aenm.201600671
36. A.A. AbdelHamid, Y. Yu, J. Yang, J.Y. Ying, Generalized synthesis of metal oxide nanosheets and their application as Li-ion battery anodes. Adv. Mater. **29**(32), 1701427 (2017). https://doi.org/10.1002/adma.201701427
37. S.L. Wang, X. Luo, X. Zhou, Y. Zhu, X. Chi et al., Fabrication and properties of a free-standing two-dimensional titania. J. Am. Chem. Soc. **139**(43), 15414–15419 (2017). https://doi.org/10.1021/jacs.7b08229
38. M. Chen, X.Z. Xiao, M. Zhang, J.F. Mao, J.G. Zheng et al., Insights into 2D graphene-like TiO_2 (B) nanosheets as highly efficient catalyst for improved low-temperature hydrogen storage properties of MgH_2. Mater. Today Energy **16**, 100411 (2020). https://doi.org/10.1016/j.mtener.2020.100411
39. Z. Hao, Q. Chen, W. Dai, Y. Ren, Y. Zhou et al., Oxygen-deficient blue TiO_2 for ultrastable and fast lithium storage. Adv. Energy Mater. **10**(10), 1903107 (2020). https://doi.org/10.1002/aenm.201903107
40. G. Ou, Y. Xu, B. Wen, R. Lin, B. Ge et al., Tuning defects in oxides at room temperature by lithium reduction. Nat. Commun. **9**, 1302 (2018). https://doi.org/10.1038/s41467-018-03765-0
41. G. Yin, X. Huang, T. Chen, W. Zhao, Q. Bi et al., Hydrogenated blue titania for efficient solar to chemical conversions: preparation, characterization, and reaction mechanism of CO_2 reduction. ACS Catal. **8**(2), 1009–1017 (2018). https://doi.org/10.1021/acscatal.7b03473
42. L. Ren, W. Zhu, Q. Zhang, C. Lu, F. Sun et al., MgH_2 confinement in MOF-derived N-doped porous carbon nanofibers for enhanced hydrogen storage. Chem. Eng. J. **434**, 134701 (2022). https://doi.org/10.1016/j.cej.2022.134701
43. C. Lu, Y. Ma, F. Li, H. Zhu, X. Zeng et al., Visualization of fast "hydrogen pump" in core–shell nanostructured Mg@Pt through hydrogen-stabilized Mg_3Pt. J. Mater. Chem. A **7**(24), 14629–14637 (2019). https://doi.org/10.1039/c9ta03038g
44. J. Yang, Y.L. Jiang, L.J. Li, E. Muhire, M.Z. Gao, High-performance photodetectors and enhanced photocatalysts of two-dimensional TiO_2 nanosheets under UV light excitation. Nanoscale **8**(15), 8170–8177 (2016). https://doi.org/10.1039/c5nr09248e
45. D. Pukazhselvan, N. Narendar, C. Pedro, C.A. Enrique, O.I. Gonzalo et al., Evolution of reduced Ti containing phase(s) in MgH_2/TiO_2 system and its effect on the hydrogen storage behavior of MgH_2. J. Power Sourc **362**, 174–183 (2017). https://doi.org/10.1016/j.jpowsour.2017.07.032
46. D. Pukazhselvan, N. Narendar, K.S. Sandhya, S. Budhendra, B. Igor et al., Role of chemical interaction between MgH_2 and TiO_2 additive on the hydrogen storage behavior of MgH_2. Appl. Surf. Sci. **420**, 740–745 (2017). https://doi.org/10.1016/j.apsusc.2017.05.182
47. D. Pukazhselvan, N. Narendar, Y. Tao, R. Devaraj, S. Aliaksandr et al., Chemically transformed additive phases in Mg_2TiO_4 and $MgTiO_3$ loaded hydrogen storage system MgH_2. Appl. Surf. Sci. **472**, 99–104 (2019). https://doi.org/10.1016/j.apsusc.2018.04.052
48. O. Friedrichs, J.C. Sánchez-López, C. López-Cartes, T. Klassen, R. Bormann et al., Nb_2O_5 "pathway effect" on hydrogen sorption in Mg. J. Phys. Chem. B **110**(15), 7845–7850 (2006). https://doi.org/10.1021/jp0574495
49. X. Chen, L. Liu, P.Y. Yu, S.S. Mao, Increasing solar absorption for photocatalysis with black hydrogenated titanium dioxide nanocrystals. Science **331**(6018), 746–750 (2011). https://doi.org/10.1126/science.1200448
50. H. Zhang, Q. Kong, S. Hu, D. Zhang, H. Chen et al., Engineering the oxygen vacancies in $Na_2Ti_3O_7$ for boosting its catalytic performance in MgH_2 hydrogen storage. ACS Sustain. Chem. Eng. **10**(1), 363–371 (2021). https://doi.org/10.1021/acssuschemeng.1c06444
51. D. Pukazhselvan, G. Otero-Irurueta, J. Pérez, B. Singh, I. Bdikin et al., Crystal structure, phase stoichiometry and chemical environment of $Mg_xNb_yO_{x+y}$ nanoparticles and their impact on hydrogen storage in MgH_2. Int. J. Hydrog. Energy **41**(27), 11709–11715 (2016). https://doi.org/10.1016/j.ijhydene.2016.04.029
52. G. Liang, J. Huot, S. Boily, A.V. Neste, R. Schulz, Catalytic effect of transition metals on hydrogen sorption in nanocrystalline ball milled MgH_2-Tm (Tm=Ti, V, Mn, Fe and Ni) systems. J. Alloys Compd. **292**(1), 247–252 (1999). https://doi.org/10.1016/S0925-8388(99)00442-9
53. J. Zhang, S. Yan, L.P. Yu, X.J. Zhou, T. Zhou et al., Enhanced hydrogen storage properties and mechanisms of magnesium hydride modified by transition metal dissolved magnesium oxides. Int. J. Hydrog. Energy **43**(48), 21864–21873 (2018). https://doi.org/10.1016/j.ijhydene.2018.10.017
54. H. Yike, A. Cuihua, Z. Qiuyu, Z. Lei, S. Huaxu et al., Cost-effective mechanochemical synthesis of highly dispersed supported transition metal catalysts for hydrogen storage. Nano Energy **80**, 105535 (2020). https://doi.org/10.1016/j.nanoen.2020.105535

 https://doi.org/10.1007/s40820-022-00891-9